metals

MDPI

Article

Comparative Study on the Microstructure and Biodegradation Behavior of Commercialized Pure Mg and Mg-1.0Ca-0.5Sr Alloy in 27 mM HCO_3^--SBF: The Influence of the pH Regulation Treatments

Sabri Shafyra [1], Engku Mohammad Nazim [1], Nor Hasrul Akhmal Ngadiman [1,2,*] and Izman Sudin [1]

[1] Faculty of Engineering, School of Mechanical Engineering, Universiti Teknologi Malaysia, Johor Bahru 81310, Johor, Malaysia
[2] Department of Engineering, Faculty of Advanced Technology and Multidiscipline, Universitas Airlangga, Surabaya 60115, Indonesia
* Correspondence: norhasrul@utm.my

Abstract: The biodegradation behavior of newly developed orthopedic implant materials provides essential insight into the potential degradation products and their ability to match the rate of bone healing prior to complete degradation. Ironically, biodegradation performance is not only influenced by alloy design or advanced surface treatment on the alloy, but also it is dominantly controlled by the specific inorganic species and their concentration in the corrosion media as well as their pH level. In this study, the biodegradation behavior of commercially pure magnesium (CP Mg) and a Mg-1.0Ca-0.5Sr alloy was evaluated in 27 mM HCO_3^- - Simulated Body Fluid (r-SBF) due to its identical ionic species and concentrations with human blood plasma via immersion test, including (i) hydrogen evolution test (H_2), (ii) pH trend, and (iii) weight-loss measurement. To simulate the pH regulation by the physiological homeostatic response, the pseudo-physiological solution was treated with two treatments: through a (i) a 24 h corrosion media renewal routine and through the use of (ii) a TRIS-HCL buffer reagent. The Mg-1.0Ca-0.5Sr alloy is shown to have superior corrosion resistance due to grain refinement and unique secondary phases, whereas the daily renewal routine imparts a better emulation of in vivo corrosion control.

Keywords: magnesium alloy; biodegradable alloy; corrosion; orthopedic implant

Citation: Shafyra, S.; Nazim, E.M.; Ngadiman, N.H.A.; Sudin, I. Comparative Study on the Microstructure and Biodegradation Behavior of Commercialized Pure Mg and Mg-1.0Ca-0.5Sr Alloy in 27 mM HCO_3^--SBF: The Influence of the pH Regulation Treatments. *Metals* **2023**, *13*, 136. https://doi.org/10.3390/met13010136

Academic Editor: Marcello Cabibbo

Received: 20 December 2022
Revised: 4 January 2023
Accepted: 6 January 2023
Published: 9 January 2023

1. Introduction

Bone fracture is conventionally treated by utilizing permanent implants made from metallic biomaterials such as titanium (Ti), 316 L stainless steel (316 L SS), and cobalt–chromium–molybdenum (Co-Cr-Mo)-based alloys [1–3]. The utilization of these orthopedic implants has been manifested as mechanically efficacious in treating a bone fracture. However, the employment of these permanent implants is associated with multiple major clinical drawbacks, including peri-implant bone loss due to the effect of stress shielding, impaired adjacent tissues caused by the release of metal ions, and unexpected pain or discomfort [4,5].

In order to fend off the risk of the stress shielding effect, a new implant material should be tailored to match the human bone's modulus. Magnesium (Mg), an existing essential element in the human physiological system, exhibits the closest match in modulus value with human bone and has high specific strength and excellent biocompatibility [6,7]. However, its rapid degradation rate may result in premature loss of mechanical properties, excessive hydrogen gas accumulation, bone resorption, and severe hemolysis [8,9]. Fortunately, the degradation behavior of Mg can be significantly altered via alloying techniques [6,10]. A few examples of alloying elements in Mg that have been extensively examined for orthopedic implant application include aluminum (Al), zinc (Zn), cadmium (Cd), nickel (Ni),

lead (Pb), and lanthanum (La). Nonetheless, in vivo testing has shown that these elements are classified as toxic and could elicit allergic reactions [10]. Because biocompatibility is the most important requirement for a successful implant, nutrient alloying elements are highly favorable in guaranteeing biosafety by promoting excellent hemocompatibility and cytocompatibility [11]. In this study, calcium (Ca) and strontium (Sr) were selected as the alloying elements. Ca, as the major component in bone structure, is responsible for bone mineralization [12]. The deployment of Ca as an alloying element can reduce hypercalcemia risk because it regulates in a similar nature to Mg [13,14]. Meanwhile, Sr is responsible for promoting bone construction and preventing bone resorption; thus it becomes beneficial in treating osteoporosis [15,16].

Generally, Simulated Body Fluid (SBF) was utilized by the majority of research groups due to its zero-contamination risk. Originally, SBF was named c-SBF, a TRIS-buffered corrosion media that contains a stark deficiency in HCO_3^- (only 4.2 mM) compared to human blood plasma (27 mM). Xin et al. studied the effects of different HCO_3^- content (4 mM, 15 mM and 27 mM) on Mg. They found that SBF with 27 mM HCO_3^- enhances pH-buffering capacity and decreases corrosion rate by generating a more uniform and compact corrosion layer. Moreover, it has been reported that the protective efficiency of the corrosion layer is largely influenced by the synergistic reaction between Ca^{2+}, Mg^{2+}, HCO_3^-, and $HPO_4{}^{2-}$.

Ironically, the majority of studies [6,17] utilized the typical c-SBF in their works. In addition, c-SBF contains a higher content of aggressive Cl^- ions (147.8–148.8 mM) compared to human blood plasma (103 mM). Moreover, Kim et al. have reported that the composition of the precipitated apatite within conventional c-SBF deviates from natural bone apatite due to the unmatched HCO_3^- and Cl^- concentrations [18–21]. Therefore, it is critical to investigate the degradation of any biomaterials in a corrosion media that is conditioned to have ionic compositions and concentrations relevant to the human body. In this study, r-SBF, or 27 mM HCO_3^- /103 mM Cl^-, were chosen as the corrosion media.

Apart from the critical selection of corrosion media when simulating the in vivo response, its pH value largely influences the formation and dissolution of the corrosion by-product. Excessive OH^- formation may shift the normal physiological pH (7.35–7.45) to a fluctuating pH. The abrupt pH changes may upset the peri-implant tissue by disrupting the protein and cell structures, thus impacting normal physiological function [17]. Therefore, it is crucial to include a buffering system in corrosion media to avoid discrepancies in biocorrosion behavior and by-products.

Tris (hydroxymethyl) aminomethane buffer (Tris-HCL), 4-(2-hydroxylethyl)-1piperazineethanesulfonic acid (HEPES), $NaHCO_3/CO_2$, and phosphate buffer solution (PBS) are frequently used as buffering reagents in corrosion media. $NaHCO_3/CO_2$ buffer is commonly recommended due to its capacity to produce a HCO_3^-/H_2CO_3 buffer. Moreover, it mimics the buffering mechanism established by respiratory control. Comparable in vivo results have been found in several studies; however, its complex set-up has made it less desirable to researchers [17]. HEPES and Tris-HCL, on the other hand, offer a simpler experiment preparation and set-up, which can regulate the pH value from 6.8 to 8.2 and 7.0 to 9.0, respectively. Despite their extensive use, HEPES and Tris-HCL do not readily exist in the human body; thus, their utilization might give a deviated biodegradation profile to an in vivo response. For this reason, a simpler approach to regulate the pH can be achieved by daily renewal of the corrosion media (24 h interval replenishment). To date, there are no comparative studies of the pH-regulating techniques on the biodegradation profile of the pure Mg and its alloy in r-SBF solutions.

This paper aims to determine the relevant in vitro corrosion media for Mg-based orthopedic implants by elucidating the effect of inorganic ion composition and concentration in pH-regulated systems. To mimic dynamic in vivo pH control, 24 h corrosion media renewal was performed and Tris/HCL buffer reagent was added to the corrosion media. Degradation kinetics and mechanisms were studied by immersion testing, which includes H_2 evolution test, pH variation assessment, and mass loss measurement. The corrosion

precipitation types and their order of formation with respect to pH value are predicted via Hydra–Medusa simulation and verified by experimental characterization of the corrosion surface and its components.

2. Materials and Methods

2.1. Sample Preparation

The CP Mg and Mg–Ca–Sr ternary alloy was cast in a sealed induction furnace (Inductotherm Ltd., Seaford, Australia) in which the alloy was adjusted to a nominal composition of 1 wt.% Ca and 0.5 wt.% Sr. The starting materials were in various forms, with the CP Mg in smaller ingots (99%, Sigma-Aldrich, St. Louis, MO, USA), whereas Ca and Sr were in granular form (99%, Sigma-Aldrich, St. Louis, MO, USA) to ensure homogeneous solidification. The oxide layer formed on the CP Mg ingot was removed with silicon carbide (SiC) abrasive paper before being ultrasonically cleaned in acetone for 10 min prior to the casting process to avoid contamination and inaccurate alloy composition. Then, all the raw materials were filled into high-purity graphite crucibles and melted at 720 °C under the protection of a high-purity Argon (Ar) gas stream. The crucible opening was plugged with a refractory clay mix to block oxygen ingress. Each melt was held for about 45 min until all of the raw materials formed a homogeneous molten alloy solution. The molten alloy was quickly poured into a preheated mild steel mold (250 °C) and air cooled. The solidified alloy was then sectioned into 10 mm × 10 mm × 4 mm thin plates for microstructural analysis purposes and disk-shaped samples of ⌀ 15 mm × 2 mm for the immersion test. The samples were surface abraded with 2000 grit SiC abrasive paper, polished, and ultrasonically rinsed in acetone for 10 min before air drying. Subsequent sample handling was performed under sterile conditions.

2.2. Microstructure Characterization

The CP Mg and its alloy were chemically etched with 2% nitric acid solution (QReC, Auckland, New Zealand) for 5 s, then washed with running water to disclose the microstructure. The air-dried CP Mg and Mg-1.0Ca-0.5Sr alloy microstructure profile variations were examined and compared using an Olympus BX60FS optical microscope (OM) (Olympus Optical Co., Ltd., Tokyo, Japan) and Hitachi S-3400N scanning electron microscope (SEM) (HITHACI, Tokyo, Japan) outfitted with energy dispersive spectrometry (EDS). The corresponding grain size was measured by ImageJ software (NIH, MD, USA) whereas the composition of formed phases was identified by Rigaku Smartlab X-ray Diffractometer (XRD) (Rigaku Corp., Tokyo, Japan).

2.3. Immersion Test

At a starting pH of 7.4, an immersion test was conducted using r-SBF or 27 mM HCO_3^-/103 mM Cl^- as the corrosion media. Per ASTM-G31-72, a Zenith Lab DK-S26 water bath (Zenith Lab Co., Ltd., Jiangsu, China) was used to maintain the temperature at 37 ± 0.5 °C for 14 days (336 h). Apart from the corrosion media, sample positioning and the ratio of the corrosion media volume to the sample's surface area (V/S) strongly influence the Mg degradation profile. Therefore, for the purpose of preventing crevice corrosion, the sample was suspended using inert fishing line (Gamakatsu Co., Ltd., Nishiwaki, Japan) [22]; meanwhile, the V/S ratio was set to 1 cm^2/40 mL to avoid a drastic and unstable pH climb during the initial immersion period [23]. The exposed r-SBF in the beaker was covered with inert cling film and further roofed with a water bath cover to avoid pH change resulting from hydrogen contamination from the ambient and to ensure one-path H_2 gas evolution leading into the burette. Figure 1 shows the experimental setup for this test. Two distinct conditions were used to regulate the pH of the r-SBF: (i) 24 h media replacement; and (ii) addition of Tris/HCl buffer reagent, with the uninterrupted system designated as the controlled system. The abbreviations for the CP Mg and Mg-1.0Ca-0.5Sr alloy in each condition are provided in Table 1 to allow for easier results comparison.

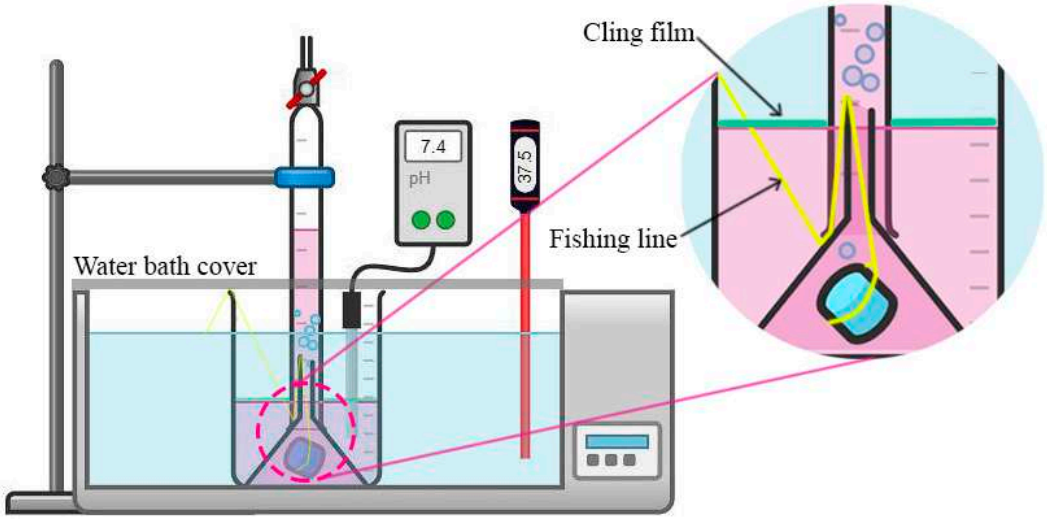

Figure 1. Schematic representation of the experimental setup for the immersion test. The sample was suspended using inert fishing line during the immersion period, with the evolved H_2 gas being calculated based on the displaced r-SBF in the burette.

Table 1. Designated abbreviations for CP Mg and Mg-1.0Ca-0.5Sr alloy in three different pH-regulating treatments in r-SBF.

	Abbreviation		
Condition	**r-SBF**		
Material	**Uninterrupted (Non-Renewed)**	**24 h Corrosion Media Renewal**	**Tris-HCL Buffered**
CP Mg	MgSBFx	MgSBFT	MgSBFT
Mg-1.0Ca-0.5Sr	M2SBFx	M2SBFR	M2SBFT

The ionic component concentrations of the r-SBF in respect to human plasma are summarized in Table 2. While the hydrogen evolution was collected using an established method, the pH reading was determined using a Sartorius PB-10 pH meter (Sartorius Corp., Goettingen, Germany) [24]. The samples were removed from the r-SBF media after the allotted immersion period, carefully cleaned with distilled water, and left to dry by air. Using XRD, SEM, and EDS, their surface morphology and corrosion product compositions were examined while taking into consideration of the compositional heterogeneity. The mass loss of the samples was weighed using Shimadzu ATY224 UniBloc Analytical Balance (Shimadzu Corp., Kyoto, Japan) (accuracy: 0.1 mg) before and after the corrosion products were removed using a chromic acid and silver nitrate solution (Merck KGaA, Darmstadt, Germany). Then, the in vitro corrosion rate in term of mass loss and H_2 evolution was calculated using this following equation:

$$CR = \Delta m / At \quad (1)$$

where A is the initial surface area of the sample in cm^2, CR is the corrosion rate in $mg/(cm^2.h)$, m is the weight loss in mg (1 mL of evolved H_2 gas = 1.083 mg of Mg for the hydrogen evolution test), and t is the immersion time in hours. The corrosion rate was set for five marks per unit.

Table 2. Concentrations of the corrosion media components as compared to the human plasma.

Ionic Species	Ionic Concentration (mM)		
	Human Plasma	r-SBF	r-SBF + Tris/HCl
Na^+	142	142	142
K^+	5.0	5.0	5.0
Mg^{2+}	1.5	1.5	1.5
Ca^{2+}	2.5	2.5	2.5
Cl^-	103	103	103
HCO_3^-	27.0	27.0	27.0
HPO_4^{2-}	1.0	1.0	1.0
SO_4^{2-}	0.5	0.5	0.5
Tris	-	-	50.5

2.4. Corrosion Precipitation Prediction via Hydra–Medusa

The Hydra–Medusa program (Royal Institute of Technology, Stockholm, Sweden) modelled potential corrosion by-product precipitation related to pH value. Of the Hydra program, all ionic components in r-SBF were defined. To forecast the potential production of corrosion deposits at various pH levels, the concentration of these components was then provided in the Medusa program. However, the ultimate ionic concentrations of Mg^{2+}, Ca^{2+}, and Sr^{2+} were computed from the evolved H_2 gas and were added to their original concentrations. To display the final potential precipitations, the simulated diagram of precipitation fraction versus pH value with regard to Mg^{2+} and Ca^{2+} was merged into a single diagram.

3. Results and Discussion

3.1. Cp Mg and Mg Alloy Microstructure and Phase Constitution Characterization

To elucidate the impact of alloying elements on the metallographic configuration of the Mg, OM, SEM, EDS, and XRD methods were used to analyze the as-cast CP Mg and Mg-1.0Ca-0.5Sr alloy. A tallied value between the nominal composition and the discovered Mg, Ca, and Sr percentages was seen, indicating the acceptability of the chosen form for the starting materials in the casting process. Table 3 summarizes the chemical composition of the as-cast CP Mg and Mg-1.0Ca-0.5Sr alloy. The microstructure of the Mg-1.0Ca-0.5Sr alloy and CP Mg differ noticeably, with the former having a single-phase structure with substantially larger grains (510 ± 22 μm), as seen in Figure 2. Due to the material's enormous grain size, the resulting XRD spectra (Figure 3) were extremely sharp and perfectly matched the pure Mg peak (JCPDS No. 98-006-221).

Table 3. Elemental comparison between the nominal content and EDS-analyzed value.

Mg System	Mg (wt.%)		Ca (wt.%)		Sr (wt.%)	
	Nominal	Detected	Nominal	Detected	Nominal	Detected
CP Mg	100.0	99.8	0	0.01	0	0
Mg-1.0Ca-0.5Sr	98.5	98.3	1.0	1.2	0.5	0.5

The as-cast Mg-1.0Ca-0.5Sr alloy, however, consolidated into amorphous ellipsoidal-shaped α-Mg dendrites with lamellar structured GBs (Figure 2b,d). Table 4 lists the elemental contents that were analyzed using EDS at various locations across the micrograph. The lamellar structure in GBs was saturated with Ca and Sr eutectic phases (point A and C), whereas the α-Mg matrix (region D) was determined to possess the largest amount of Mg. A random distribution of Ca and Sr intermetallic phases was also traced in the dendritic region, in which the fraction of Sr-rich Mg predominates. It appears as a bright globular particle (point E), whereas the elements detected in the greyish globular phase (point B) are only Mg and Ca. The phases for the corresponding points in Table 4 are identified according to the Mg-1.0Ca-0.5Sr alloy thermodynamic ternary-phase diagram [25]. The

XRD spectrum of the CP Mg and Mg-1.0Ca-0.5Sr alloy is shown in Figure 3, which attests to the presence of the anticipated phases, with a visible volume fraction of secondary phases quantified as Mg_2Ca and $Mg_{17}Sr_2$ at 0.63% and 0.22%, respectively. These outcomes were consistent with the published reports [26,27].

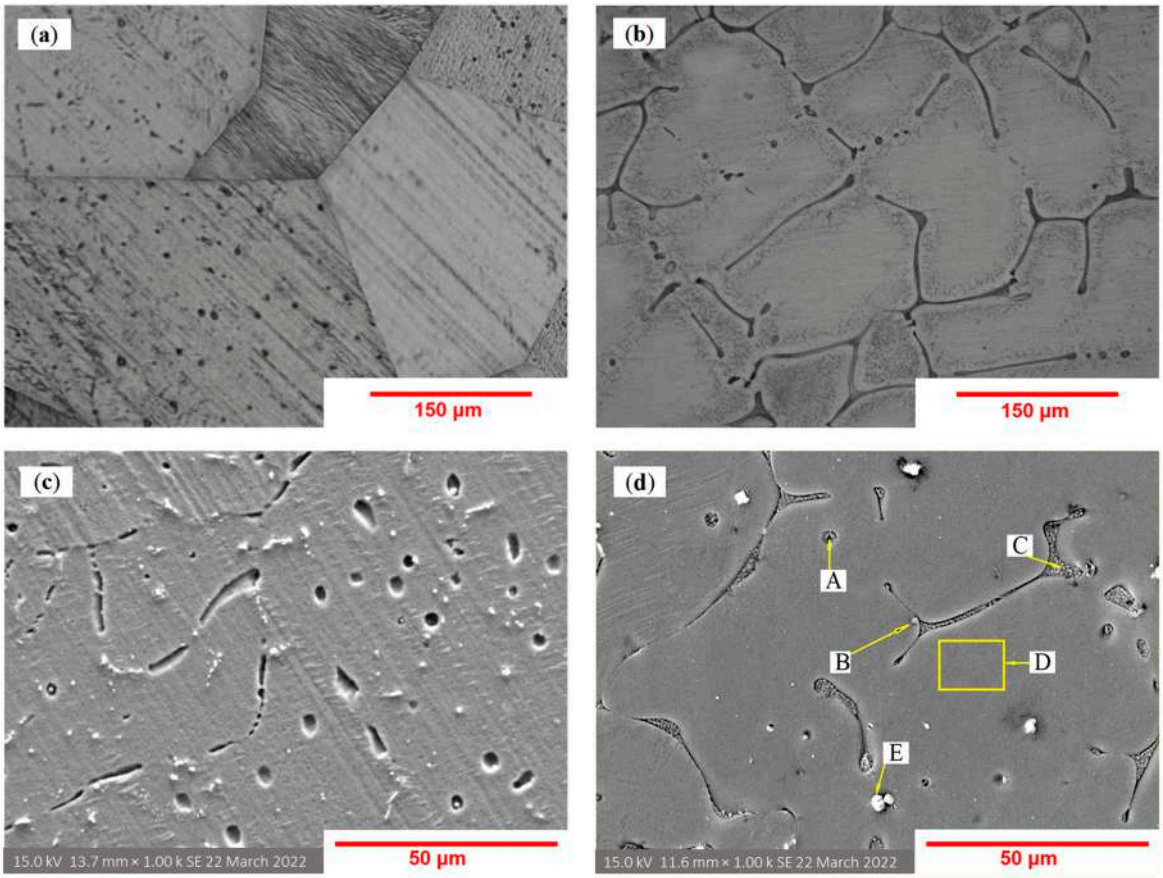

Figure 2. Optical microstructure of (**a**) CP Mg and (**b**) Mg-1.0Ca-0.5Sr alloy and their corresponding SEM images of (**c**) CP Mg and (**d**) Mg-1.0Ca-0.5Sr alloy. The marked yellow points and areas (A–E) in SEM images correspond to the EDS analysis locations in (Table 4).

Table 4. Analysis of the Mg-1.0Ca-0.5Sr alloy's chemical composition using EDS analysis and phase prediction using the modelled Mg–Ca–Sr thermodynamic phase diagram [25].

Analysis Site	Detected Element (wt.%)			
	Mg	Ca	Sr	Phase
A (globular lamellar)	65.8	9.3	24.9	Mg_2Ca and $Mg_{17}Sr_2$
B (greyish globular phase)	33.7	66.3	0	Mg_2Ca
C (GB interior)	65.0	15.0	20.0	Mg_2Ca and $Mg_{17}Sr_2$
D (α-Mg interior)	99.5	≈0	≈0	Mg
E (bright globular particle)	75.3	0	24.7	$Mg_{17}Sr_2$

The introduction of both Ca and Sr into the Mg system dramatically reduced the grain size to 96 ± 10 µm. This refinement effect was due to the enrichment of the solute undercooling (ΔT), in which its pivotal influence on the as-cast grain size and intermediate phase formation was correlatively described via the growth restriction factor (GRF), Q [28]. A higher ΔT at the front of the developing dendritic is indicated by a higher Q value [29]. Because Ca and Sr have relatively low solubility limits in α-Mg (1.34 wt.% and 0.11 wt.%, respectively), they were quickly enriched in the front of the solid/liquid interface as a result of rejecting the alloying elements, which prevented grain growth during solidification [30,31].

In this work, Q_{total} for Mg-1.0Ca-0.5Sr alloy had a significant contribution from $Q_{1.0Ca}$; the growth restriction factor of $Q_{1.0Ca}$ (11.9098) is higher than that of $Q_{0.5Sr}$ (1.75441), suggesting that 1.0 wt.% Ca had a dominant impact on grain refinement. Prior studies also revealed that Ca had a similar effect on grain-refining [32–35].

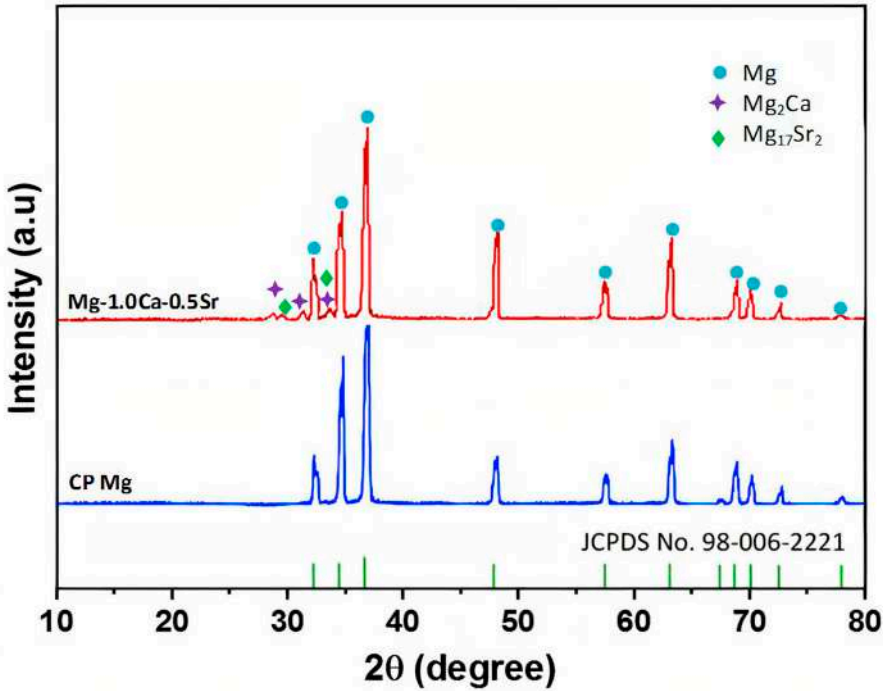

Figure 3. The XRD spectra of as-cast CP Mg and Mg-1.0Ca-0.5Sr alloy.

3.2. Post-Immersion: Morphology Analysis and Corrosion Precipitation Characterization

Figure 4 displays the corrosion morphologies of the CP Mg and Mg-1.0Ca-0.5Sr alloy in conditioned r-SBF. Both qualitative and quantitative comparisons were made between impacts of the CP Mg and Mg-1.0Ca-0.5Sr alloy on the corrosion profile under various pH regulation techniques.

During the 14-day immersion period, the CP Mg and Mg-1.0Ca-0.5Sr alloy exhibits a varying morphology of the corrosion deposits. In Figure 4a, MgSBFx displays a mixed morphology in which the corrosion precipitate appeared spiky and sandy as well as flat and cracked. Interestingly, a needle-like cluster can be seen at point A where the Ca to P (Ca:P) ratio identified via EDS analysis in Table 5 is 1.673, which corresponds to the pure stochiometric ratio of bone-like mineral known as hydroxyapatite (HA) or $Ca_5(PO_4)_3(OH)$ [36,37]. However, the thick flat surface with a visible crack in area B is identified as $Mg(OH)_2$. The dehydration of the precipitates during the sample-preparation process before the SEM examination, which involved the drying stage, could likely be the reason for the crack formation [38].

In the renewed r-SBF treatment Figure 4b, the primary constituents in the C region are Mg, O, C, and Ca, whereas point D contains a distinctly high amount of Mg. This result was confirmed via XRD analysis in Figure 5, which shows that Mg, $MgCO_3$, $Mg(OH)_2$, and HA peaks were detected. Despite the rapid corrosion rate of CP Mg and the continuous supply of corrosive Cl^- ions, neither deep grooves nor pits were found on the MgSBFR. This is in contrast to the findings of Xin et al., who reported an increased probability of localized degradation with increasing Cl^- concentration in HCO_3^- - deficient m-SBF (HCO_3^- = 4.2 mM) [39]. The absence of localized corrosion in this study suggests that r-SBF with a carbonate concentration similar to blood plasma (27 mM) has improved the corrosion resistance of the Mg alloy.

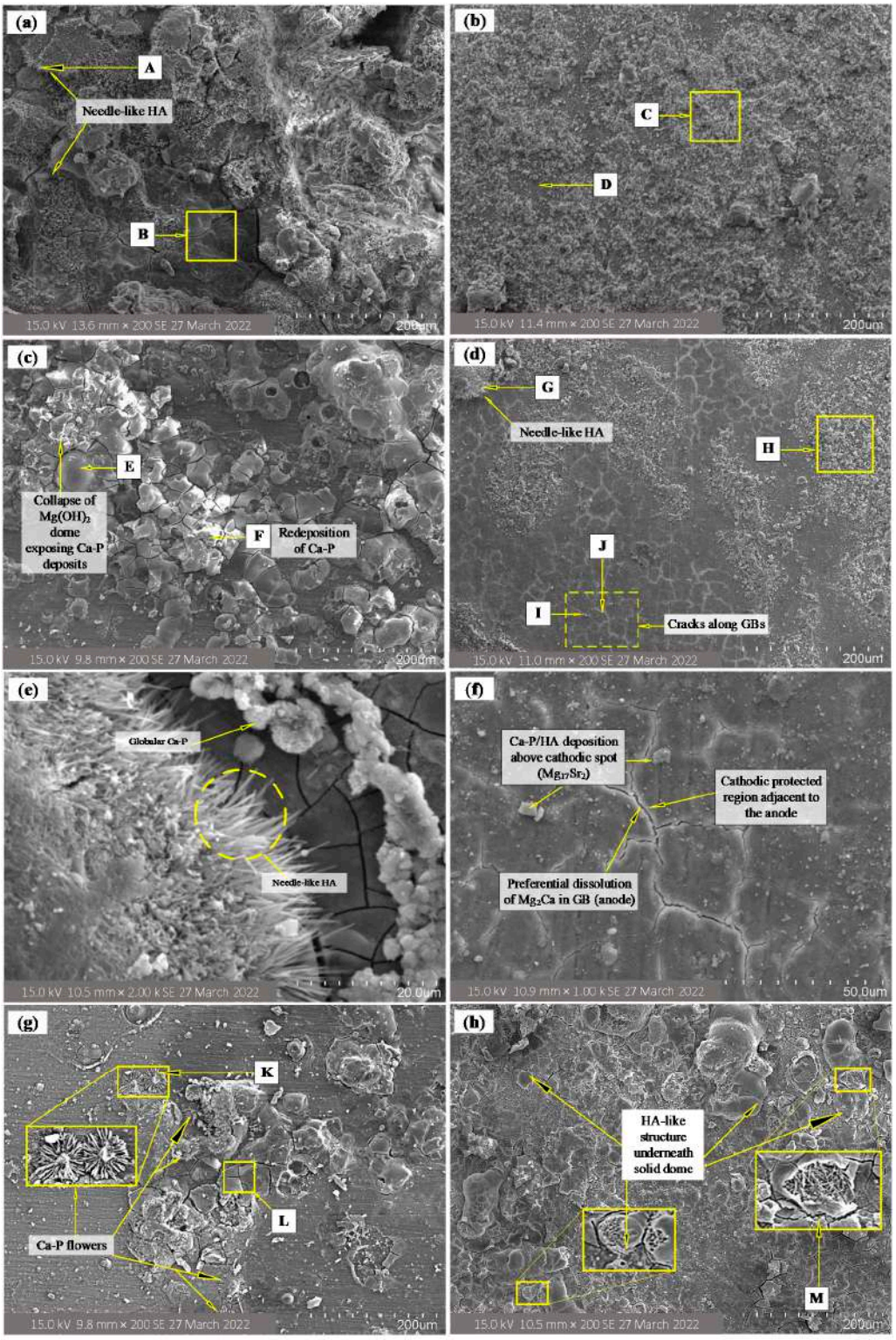

Figure 4. SEM image of deteriorated surface of CP Mg and Mg-1.0Ca-0.5Sr alloy in r-SBF under different pH regulation treatment. CP Mg in (**a**) uninterrupted r-SBF solution, MgSBFx; (**b**) interrupted r-SBF solution, MgSBFR; and (**c**) Tris-HCL buffered r-SBF solution, MgSBFT. Mg-1.0Ca-0.5Sr alloy in (**d**) uninterrupted r-SBF solution, M2SBFx; (**g**) interrupted r-SBF solution, M2SBFR; and (**h**) Mg-1.0Ca-0.5Sr alloy in Tris-HCL buffered r-SBF solution, M2SBFT. The images (**e**,**f**) show a magnified perspective of the dotted square and needle-like HA structure in (**d**). The annotated yellow points and areas (A–M) in SEM images correlate to the locations of the EDS analysis (Table 5).

Table 5. Elemental composition of CP Mg and Mg-1.0Ca-0.5Sr alloy corrosion product via EDS analysis. Spots and area analysis (A–M) are indicated in Figure 4.

Material	Analysis Site	Elements (at.%)							Ca:P
		Mg	O	C	Cl	Ca	Sr	P	
MgSBFx	A	5.4	60.9	19.8	-	8.7	-	5.2	1.673
	B	6.2	58.1	18.9	-	7.2	-	10.3	0.699
MgSBFR	C	18.9	49.1	9.5	-	11.2	-	10	1.120
	D	58.1	11.6	12.4	-	5.1	-	12.8	0.398
MgSBFT	E	22.4	71.8	5.8	-	-	-	-	-
	F	12.8	68.3	7.3	0.5	6.3	-	4.8	1.312
M2SBFx	G	4.80	72.4	6.5	-	9.4	0.3	5.6	1.678
	H	25.4	63.4	11.5	0.2	8.3	0.5	6.9	1.203
	I	3.2	41.3	20.5	-	20.5	0.1	14.4	1.423
	J	10.2	68.2	9.5	-	5.3	0.2	6.6	0.803
M2SBFR	K	8.7	63.6	13.5	-	8.1	0.1	6	1.350
	L	23.8	71.2	4.9	0.1	-	-	-	-
M2SBFT	M	5.7	52.4	19.3	0.4	7.2	0.1	4.3	1.674

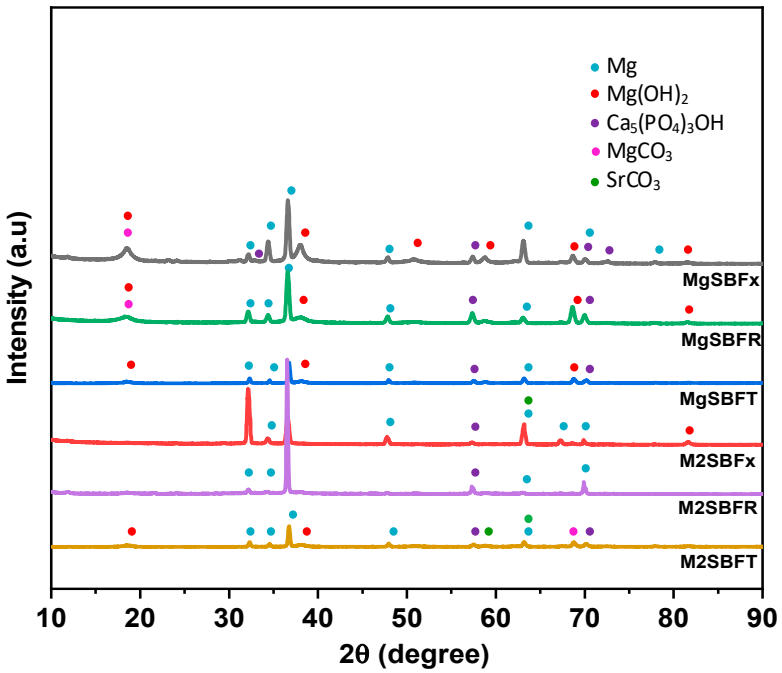

Figure 5. XRD peaks of CP Mg and Mg-1.0Ca-0.5Sr alloy after 14-day immersion in r-SBF corrosion media under different pH control conditions.

However, multiple blisters or volcano-like craters appeared in the Tris-HCL buffered r-SBF solution (Figure 4c). At point F, redeposition of corrosion deposits was observed, and this deposit was identified as calcium phosphate (CaP) with a Ca:P ratio of 1.312. However, the dome and the thick flat deposits have since been identified as $Mg(OH)_2$ based on their analyzed atomic percentage in the EDS analysis at point E.

An apparent improvement in corrosion resistance was observed in the Mg-1.0Ca-0.5Sr alloy in r-SBF (Figure 4d–h), in which a lower degree of degradation was observed as compared to CP Mg. In Figure 4d,f, the anodic secondary phase saturated within GBs was demonstrated by the dissolved GBs network and the formation of white primer deposits adjacent to it, indicating the occurrence of preferential corrosion mechanisms due to accelerated micro-galvanic corrosion. Evident simultaneous H_2 evolution and the

preferential accumulation of OH^- bubbles at the cathodic sites on the Mg-1.0Ca-0.5Sr alloy surface was clearly evident in Figure 6.

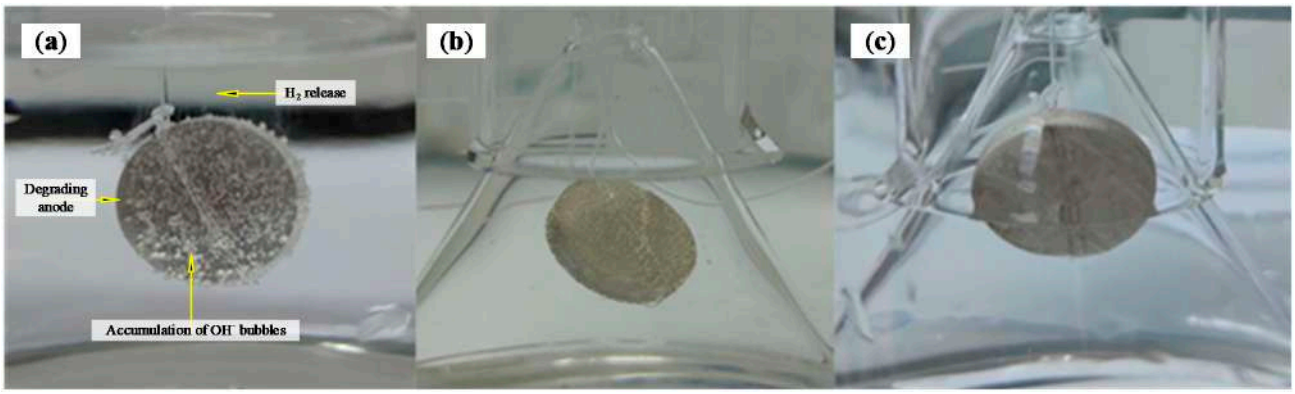

Figure 6. Photograph of Mg-1.0Ca-0.5Sr alloy immersed in r-SBF with increasing immersion time. (**a**) Rapid anodic dissolution during early immersion results in higher OH^- accumulation over the cathodic area during the earliest 1 h immersion; (**b**) slower anodic dissolution and reduced OH^- accumulation were observed at 48 h, indicating active precipitation of corrosion products on the alloy surface; and (**c**) unnoticeable OH^- accumulation at the increased immersion time (336 h), suggesting a uniform coverage of passivating deposits across the alloy's surface at 336 h.

This observation supports the widely accepted theory that accelerated Mg degradation in aqueous media generates H_2 gas and precipitates $Mg(OH)_2$ simultaneously (Equations (2)–(5)) [40,41].

$$Mg \rightarrow Mg^{2+} + 2e^- \text{ (anodic partial reaction)} \quad (2)$$

$$2H_2O + 2e^- \rightarrow H_2 + 2OH^- \text{ (cathodic partial reaction)} \quad (3)$$

$$Mg^+ + 2H_2O \rightarrow Mg^{2+} + 2OH^- + H_2 \text{ (overall reaction)} \quad (4)$$

$$Mg^{2+} + 2OH^- \rightarrow Mg(OH)_2 \text{ (corrosion product)} \quad (5)$$

The secondary phases produced in the Mg-1.0Ca-0.5Sr alloy were identified as Mg_2Ca and $Mg_{17}Sr_2$ using XRD analysis. Although most research implies that Mg_2Ca operates as an anode [42–44], there are various contradictory theories about Mg_2Ca's potential role in galvanic corrosion [45,46]. According to Kim et al., Mg_2Ca possesses a cathodic characteristic in comparison to the α-Mg matrix [47]. Xu et al., on the other hand, reported a negligible potential difference between the α-Mg matrix and Mg_2Ca [48]. However, the anodic character of Mg_2Ca is clearly demonstrated in this study (Figure 4f), in which the Mg_2Ca in GBs preferentially corrodes, whereas the nearby α-Mg becomes cathodically protected via the creation of a thin white hydroxide layer next to the anodic GBs.

$Mg_{17}Sr_2$, on the other hand, appears in both GBs as well as in the α-Mg matrix. There is also disagreement on $Mg_{17}Sr_2$'s electropotential nature. For instance, Thekkepat et al. computed the electrochemical potentials of Mg and $Mg_{17}Sr_2$ using the Born–Haber cycle and concluded that $Mg_{17}Sr_2$ serves as an anode due to its lower electrochemical potential ($E_{Mg} = -2.37$ V and $E_{Mg17Sr2} = -2.387$ V) [49]. Liu et al. provided experimental evidence for this conclusion, demonstrating that $Mg_{17}Sr_2$ preferentially corrodes and releases Sr^{2+} ions into the corrosive media [50]. However, multiple studies demonstrated the superior nature of $Mg_{17}Sr_2$ over Mg, as the neighboring α-Mg matrix rapidly disintegrated, leaving $Mg_{17}Sr_2$ at the GBs [49,51]. Nonetheless, this study supported the latter assertion. Because Mg_2Ca is the most anodic phase relative to α-Mg matrix and $Mg_{17}Sr_2$, it corroded preferentially, leaving $Mg_{17}Sr_2$ as the matrix skeleton. The increased potential of $Mg_{17}Sr_2$ changes the previously cathodic α-Mg matrix into an anodic mode in which corrosion is propagated from the region close to $Mg_{17}Sr_2$ to its core. This corrosion spread may result in the creation of shallow surface craters. The region with a high volume fraction of $Mg_{17}Sr_2$ could shield

the Mg matrix from further deterioration due to the continuous $Mg_{17}Sr_2$ network acting as a corrosion barrier [51].

In addition to the obvious effect of the alloying process on corrosion morphology, the pH treatment has an impact on it as well. In Figure 4d, several clusters of sandy deposits can be detected on the M2SBFx, whereas other areas remain uncovered, showing that the dissolution–deposition cycle during the 14-day immersion was substantially slower than the thick and rough corrosion deposit in MgSBFx. Likewise, a cluster of needle-like precipitation has formed at point G on the M2SBFx surface as it formed at point M in MgSBFx surface. This is an intriguing observation, as it suggests that the needle-like HA with a stoichiometric Ca:P ratio is more likely to form under uninterrupted media than under pH-drifting conditions generated by the renewal treatment.

This hypothesis is validated by the evidence in Figure 4g, which shows that the needle-like HA structure was absent on the M2SBFR but exhibited a different structure that resembling a daisy-like figure. The daisy-like petal (point K) identified by EDS spot analysis as CaP with a Ca:P ratio of 1.35, which falls in the β-tricalcium phosphate (β-TCP) structural range. However, similar to the previous finding, the flat deposits were identified as $Mg(OH)_2$. In addition, the superior corrosion resistance provided by Ca and Sr as alloying elements has been demonstrated in this figure, which shows that polishing striations are still visible on M2SBFR even after the 14-day immersion period, and thicker corrosion deposits are present, which was probably facilitated by the increased mass transport implicated by the partial breakdown of the corrosion layer during the renewal process [52].

The typical corrosion morphology in Tris-HCL buffered corrosion media was observed in Figure 4h. However, better coverage of the corrosion layer on Mg-1.0Ca-0.5Sr alloy was observed such that there are no visible bare Mg substrate areas on its surface, and less formation of $Mg(OH)_2$ domes was established. Intriguingly, the collapsed domes have exposed the needle-like HA structure (Ca:P = 1.674), which once again supports the previous hypothesis on the influence of pH regulation on the CaP precipitation kinetics and structures. In addition, the findings from this study were different from those of Ascensio and Ida S. Berglund; neither CaP or HA structures were revealed underneath the collapsed $Mg(OH)_2$ dome [27,52]. Furthermore, several studies have proposed the same hypothesis; $Mg(OH)_2$ forms immediately upon immersion, followed by the formation of CaP and HA [53–56]. In contrast, in this study, CaP and HA were revealed under the $Mg(OH)_2$ domes, which clearly highlights that CaP and HA may be actively formed before $Mg(OH)_2$ in r-SBF. However, the variation of the corrosion deposits and their structure across different studies has proven that the mechanism of precipitation on the Mg surface is rather stochastic, such that the sequence on which type of corrosion product is formed first is unpredictable. Therefore, the types of corrosion precipitation with respect to the ionic components and their compositional concentration are predicted via Hydra–Medusa simulation software in the following section.

As mentioned, the increase of the pH value in corrosion media was due to the generation of OH^- from Mg dissolution. Meanwhile, Tris-HCL regulates the corrosion media's pH value by consuming the generated OH^- ions from Equation (3) by its bonded H+, hence suppressing the formation of $Mg(OH)_2$ precipitates that requires OH^- ions (Equation (5)) [57,58]. This reaction, therefore, suggests that the addition of Tris-HCL in r-SBF may have severely degraded both the CP Mg and Mg-1.0Ca-0.5Sr alloy due to continuous surface activation via OH^- consumption. Ironically, in M2SBFT, there was no evidence of bare surface, which might contradict the OH^- consumption tendency imposed by the Tris-HCL buffer reagent observed in MgSBFT. There are multiple contributing factors that explain these varying surface profiles. The accumulation of excessive OH^- ions due to the fast degradation of CP Mg provides a sufficient OH^- ion supply that leads to a thicker $Mg(OH)_2$ precipitation. However, the preferential precipitation of $Mg(OH)_2$ on the existing CaP deposits rather than on the Mg substrate was due to the cathodic nature of CaP as compared to Mg. In addition, the Tris-HCL buffer reagent has ion-chelating properties such that it carries away Mg^{2+} ions from reacting with OH^- ions at the substrate's surface.

Meanwhile, the absence of a bare surface in M2SBFT was attributed to the depletion of the Tris-HCL buffer reagent towards the end of the immersion time, whereas the OH^- ions were continuously produced, thus allowing $Mg(OH)_2$ to precipitate. Moreover, the precipitation of $Mg(OH)_2$ prior to Tris-HCL depletion may have been caused by the ineffective Tris-HCL buffer reagent, in which it regulates pH in the bulk corrosion media rather than the local pH at the CP–Mg interface [57].

It must be noted, however, that the degree of corrosion to which metals are subjected cannot be judged based merely on the amount of precipitation coverage. For instance, a scarcity of passivation layer coverage may signify poorer corrosion protection in addition to indicating a delayed degradation or enhanced corrosion resistance. Therefore, the post-immersion surface evaluation must be supported by the H_2 evolution test and mass loss measurement.

3.3. Influence of pH Regulation Approaches in r-SBF

Figure 7a illustrates the volume of evolved H_2 against immersion time for the CP Mg and Mg-1.0Ca-0.5Sr alloy in r-SBF under three treatment settings. The H_2 evolution test is an excellent yet straightforward technique for evaluating the in vitro corrosion rate of metals in aqueous media. Because the dissolution of Mg is accompanied by a pH change, the H_2 evolution test is supplemented by the pH trend test (Figure 7b) in order to reflect the corrosion rate and behavior of each metal in different pH regulation treatments. It is broadly accepted that the dissolution of Mg generates OH^- ions, which shift the pH of the system to a higher basic level [59,60]. Meanwhile, Figure 7c displays the calculated degradation rate in term of released H_2 volume and mass loss.

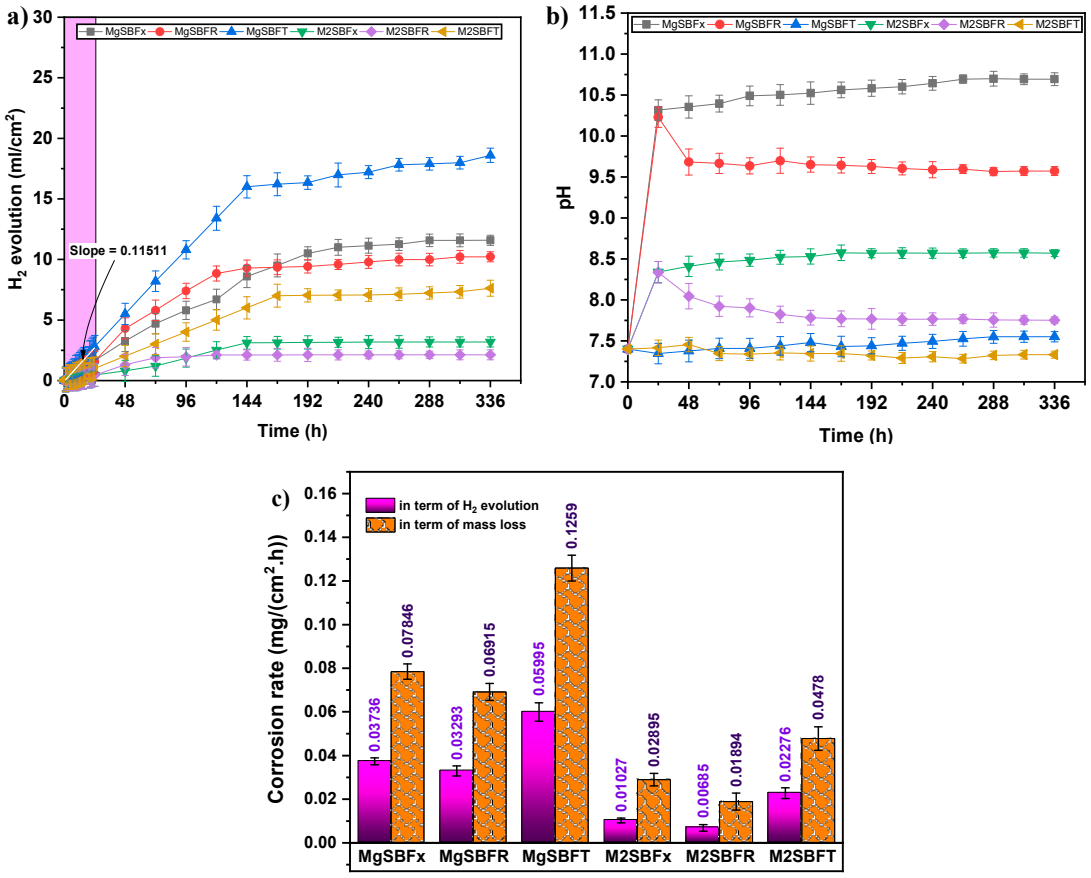

Figure 7. Immersion test results of CP Mg and Mg-1.0Ca-0.5Sr alloy in r-SBF corrosion media. (**a**) H_2 evolution curves in different pH-regulating treatments, (**b**) time dependant pH change, and (**c**) corrosion rate in terms of mass loss and evolved H_2 (The legends in (**a**,**b**) indicate the respective materials in corresponding corrosion media and treatment condition, as summarized in Table 1).

From Figure 7a, both the CP Mg and Mg-1.0Ca-0.5Sr alloy follow an identical evolution trend under all treatment conditions, in which abrupt H_2 release was observed in the early immersion phase, suggesting rapid dissolution of the anode which is striving for a dynamic equilibrium state [56]. Then, the H_2 release slowed down before reaching a stabilized evolution rate. This profile may be attributed to the gradual growth of protective precipitation coverage across the surface, except for MgSBFT and M2SBFT, in which a continuous climb was seen until the end of immersion period.

From Figure 7b,c, a hypothesis can be derived that the lower pH value in r-SBF could be a mark of better corrosion resistance. This is due to the multiple passivation provided by the Mg^{2+}, Ca^{2+}, HCO_3^-, and $HPO_4{}^{2-}$ species within r-SBF that form CaP and HA that starts at a lower pH [6], rather than only depending on the reaction of Mg^{2+} and OH^- to form $Mg(OH)_2$. In addition, M2SBFT exhibits lower pH value than MgSBFT, indicating better corrosion resistance induced by the alloying elements, which is in accordance with the results in the H_2 evolution test and mass loss measurement. However, this hypothesis is not applicable when comparing the treatment conditions with Tris-HCL buffered r-SBF.

In the renewed r-SBF treatment, a different pH trend curve was observed, with the CP Mg and Mg-1.0Ca-0.5Sr alloy exhibiting a prompt pH drop from pH 10.23 to 9.68 and pH 8.34 to 8.05, respectively, (hour 24 to 48). This trend has established a correlation between corrosion rate or H_2 evolution and the pH variation such that the intermittent deterioration of protection coverage occurs after each renewal process. According to Equation (6), the solubility equilibrium of $Mg(OH)_2$ was influenced by the pH value [52,61];

$$\text{Log } [Mg^{2+}] = 16.95 - 2\text{pH} \quad (6)$$

For instance, the pH values of CP Mg and Mg-1.0Ca-0.5Sr in renewed r-SBF exhibit a prompt pH drop from pH 10.23 to 9.68 and pH 8.34 to 8.05, respectively, which has increased the $Mg(OH)_2$ solubility which leads to the passivation breakdown. This corrosion protection layer breakdown exposes the Mg substrate back to the mass corrosion attack. In addition, the daily renewal of the corrosion media has caused an increased Cl^- attack on $Mg(OH)_2$, transforming the hydroxide layer into a highly soluble $MgCl_2$, as in the following equation [62]:

$$Mg(OH)_2 + 2Cl^- \rightarrow MgCl_2 + 2OH^- \quad (7)$$

However, the pH started to reach a plateau despite the corrosion-media-renewal routine at hour 168 onwards. This may be attributed to the increased volume of secondary hydroxide precipitation and the additional corrosion barrier formation produced from the components in the r-SBF [63–65]. It is shown in Figure 8 that HA and $MgCO_3$ dominates at lower and intermediate pH levels, and their precipitation reactions are as follows [61,66]:

$$5Ca^{2+} + 3PO_4{}^{3-} + OH^- \rightarrow Ca_5(PO_4)_3OH \quad (8)$$

$$HCO_3^- + OH^- \rightarrow CO_3^{2-} + H_2O \quad (9)$$

$$2Mg^{2+} + CO_3{}^{2-} + 2OH^- \rightarrow MgCO_3 + MgOH_2 \quad (10)$$

The absence of pH increase effect in renewed r-SBF was attributed to the formation of HA and $MgCO_3$ that consumed OH^- during their formation as well as due to the stable and insoluble properties which act as the barrier against Cl^- infiltration. This is confirmed by the fact that no trace of pitting corrosion was visible on the r-SBF treated materials, which is in agreement with the Xin et al. finding that the formation of pitting was suppressed by the formation of Mg carbonates [67]. However, the XRD peak of $MgCO_3$ for both the CP Mg and Mg-1.0Ca-0.5Sr alloy is observed to have minimal to no peak due to the buildup of $Mg(OH)_2$, despite their simultaneous precipitation (Equation (10)). This is due to the using up of HCO_3^- ions at the final immersion period, whereas Mg^{2+} and OH^- were produced continuously [61].

In addition, the increase in $Mg(OH)_2$ thickness led to its dehydration at the $Mg(OH)_2$/Mg interface due to restricted corrosion media absorption, thereby converting the formed $Mg(OH)_2$ to MgO [52,68,69];

$$Mg(OH)_2 \rightleftharpoons MgO \pm H_2O \quad (11)$$

This formation of MgO underneath the $Mg(OH)_2$ layer has further blocked the infiltration of corrosive media to the Mg substrate, hence causing the pH trend to reach a quasi-constant state at longer immersion time [68]. Meanwhile, with the absence of r-SBF renewal, the pH value increases significantly at hour 24 onwards and gradually increases until it reaches a quasi-static pH value. However, the H_2 evolution trend of MgSBFR and M2SBFR started to be lower than MgSBFx and M2SBFx at hours 168 and 96, respectively, indicating an improved corrosion resistance. A study on the corrosion behavior of the CP Mg and Mg-1.0Ca-0.5Sr alloy in r-SBF under different pH-regulating conditions showed a different outcome, that is, the renewal routine of r-SBF does not decrease but improves the corrosion resistance due to the protective build-up layer formed by the constant supply of Mg^{2+}, Ca^{2+}, HCO_3^-, and HPO_4^{2-} species during the r-SBF renewal routine.

As can be seen in Figure 7c, the trend of the corrosion rate in terms of mass loss is coherent with the corrosion rate calculated from the released H_2 volume, despite their noticeable value difference. Two contributing factors to these discrepancies are as follows: (i) the overestimated corrosion rate in terms of mass loss is due to severe dislodge of the corrosion layer along with the metal substrate during chromic acid cleaning, which results in excessive mass reduction [52], and (ii) the water displacement resulting from the released H_2 may be underestimated due to the challenging H_2 gas collecting procedure due to the trapped H_2 gas within the dome-like structure. The corrosion rate of CP Mg and Mg-1.0Ca-0.5Sr in 0.9 wt.% NaCl ranked in the following decreasing order: MgSBFT > MgSBFx > MgSBFR > M2SBFT > M2SBFx > M2SBFR.

3.4. Influence of r-SBF and pH Regulation Technique on the Formation of Corrosion Protective Layer

The magnitude of corrosion resistance of any metal lies on the nature or types of corrosion precipitation that form on its surface. The prediction of the corrosion precipitation variants and their order of formation during the immersion test was simulated via Hydra–Medusa software. Figure 8 depicts the Hydra–Medusa diagrams for CP Mg and its alloy in r-SBF immersion systems. It is evident that the system with the lowest cumulative evolved H_2 has shown a lower pH value to initiate the precipitation of protective layers such as $Ca_5(PO_4)_3OH$, $MgCO_3$, and $CaCO_3$. This trend is in line with the hypothesis in the previous section, that is, that the lowest pH curve in r-SBF (without TRIS/HCL addition) indicates superior corrosion resistance. The CP Mg and Mg-1.0Ca-0.5Sr alloy exhibits an enhanced corrosion resistance due to the lower solubility of $Ca_5(PO_4)_3OH$ and the insoluble nature of the $MgCO_3$ layer. In Figure 7a,c,e, the corrosion protection at lower pH (pH 6.27 to 11.55) is dominated by the formation of $MgCO_3$ such that this precipitation was shown to be highest in the MgSBFx, MgSBFR, and MgSBFT system. This finding is in agreement with the XRD analysis in which $MgCO_3$ peaks were detected. This simulated finding also explains why a thin layer of corrosion product in Figure 6c was sufficient to prevent further deterioration and, as a result, considerably limit H_2 evolution. In addition, as mentioned, each corrosion layer is initiated at a distinct pH. For instance, HA forms initially and $Mg(OH)_2$ forms later at higher pH values. This discovery explains the development of a structure resembling a needle beneath the collapsed structure of a dome, indicating its formation sequence. Table 6 summarized the predicted precipitates for the CP Mg and Mg-1.0Ca-0.5Sr alloy in r-SBF under different immersion conditions, which is in accordance with the XRD analysis in Figure 5.

Table 6. Summary of possible precipitate predictions via Hydra–Medusa software.

System	Hydra–Medusa: Predicted Precipitation.				
	$Mg(OH)_2$	$MgCO_3$	$Ca_5(PO_4)_3(OH)$	$CaCO_3$	$SrCO_3$
MgSBFx	✓	✓	✓	✓	
MgSBFR	✓	✓	✓	✓	
MgSBFT	✓	✓	✓	✓	
M2SBFx	✓	✓	✓	✓	✓
M2SBFR	✓	✓	✓	✓	✓
M2SBFT	✓	✓	✓	✓	✓

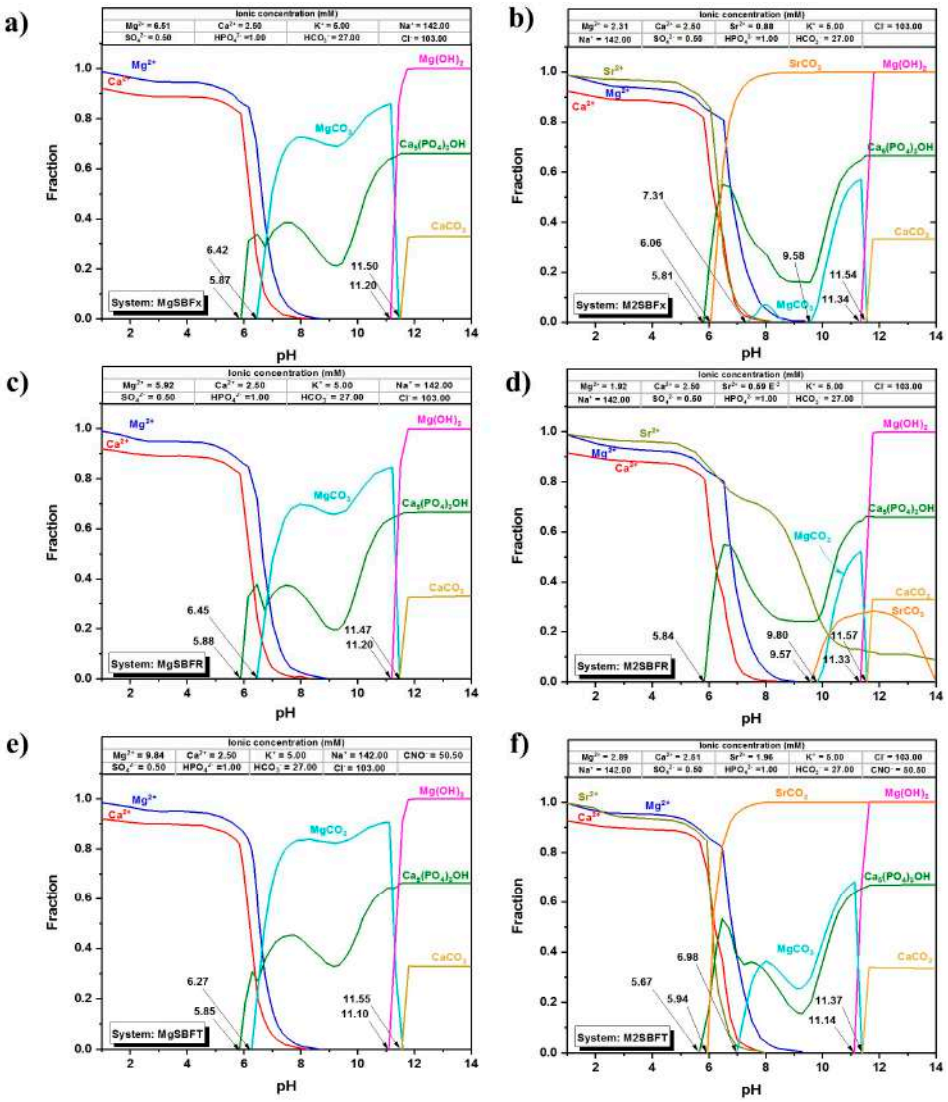

Figure 8. Simulated Hydra–Medusa diagram of either Mg^{2+}, Ca^{2+}, or Sr^{2+} fraction against pH value based on thermodynamic constant. (**a**,**c**,**e**) display the simulated diagram with predicted corrosion products of CP Mg in r-SBF solution under three treatment conditions. (**b**,**d**,**f**) illustrate the possible precipitate that resulted from Mg-1.0Ca-0.5Sr alloy immersion. The labelled pH values indicate the minimum pH value to initiate the formation of $Mg(OH)_2$, $Ca_5(PO_4)_3OH$, $MgCO_3$, $CaCO_3$, and $SrCO_3$. The summarized possible corrosion products in different corrosion media and pH-regulating conditions are listed in Table 6.

3.5. Influence of Tris-HCL Buffering Reagent

Tris-HCl is widely used in SBF solution in order to regulate the pH variation at the acceptable physiological value. As mentioned, the increase of the pH value in corrosion media was due to the generation of OH^- from Mg dissolution. Meanwhile, Tris-HCL regulates the corrosion media's pH value by consuming the generated OH^- ions in Equation (3) by its bonded H^+, hence suppressing the formation of precipitates that require OH^- ions (Equations (5), (8), and (10)) [57,58]. This reaction, therefore, suggests that the addition of Tris-HCL in both saline and r-SBF solution has resulted in deleterious corrosive attack due to continuous surface activation [70]. In addition, Tris is known as a strong chelating agent which forms weak complexes with the dissolved cations within the corrosion media, deviating the cations away from the Mg surface and, hence, delaying and inhibiting the precipitation of protective layer [6,71].

Di Mei et al. reported that Tris can still cause a detrimental corrosion to Mg even without the OH^- collecting capacity, which proves that the effect of complexation between Tris and dissolved cations such as Ca^{2+} and Mg^{2+} dominantly accelerates the degradation rate of Mg [6]. However, the detrimental effect of Tris-HCL starts to diminish after an extended amount of time, such that the precipitation of $Mg(OH)_2$ near the end of immersion period is prompted. However, this precipitation may be formed earlier due to the incapability of the synthetic buffering reagent to control a stable pH (consume OH^-) in the Nernstian diffusion layer, which explains the formation of dome-like structures in all Tris-HCL buffered systems [6]. Therefore, this phenomenon explained why there are non-uniform precipitations or lack of protection area in all the systems that involved Tris-HCL buffering agent.

In addition, despite the chelating effect of Tris-HCL on Ca^{2+}, the CaP deposition and the needle-like HA structure was observed in Figure 4c,f which can be attributed to these two respective factors: (i) the deposition of CaP deposits on top of the $Mg(OH)_2$ in MgSBFT was due to the consumed Tris-HCl at the final immersion time, allowing the Ca^{2+} ion from the r-SBF to form CaP precipitate; and (ii) the immediate formation of the HA structure in M2SBFT due to the release of Ca^{2+} through the dissolution of Mg_2Ca at the anodic GBs.

3.6. Corrosion Mechanisms of Mg-1.0Ca-0.5Sr Alloy in r-SBF

Figure 9 is a schematic illustration on the effect of r-SBF on the corrosion mechanism of the Mg-1.0Ca-0.5Sr alloy. The lamellar structure within GBs was depicted in two colors to visualize the mixed phases, with yellow representing the $Mg_{17}Sr_2$ phase and black representing the dispersion of Mg_2Ca. In the r-SBF immersion test, it is evident that the ionic species dominantly influences its corrosion profile. In Figure 9a, Mg_2Ca acts as a sacrificial anode where it preferentially dissolves, leaving the adjacent α-Mg protected. In this corrosion media, HA was formed by the reaction between Ca^{2+}, PO_4^{3-}, and OH^- ions. HA is easily precipitated in our alloy due to the readily dissolved Ca^{2+} at the surface as well as the buffering effects given by the HCO_3^- ions. However, the cathodic $Mg_{17}Sr_2$ at the front of the GBs accelerated the degradation of the neighboring α-Mg. As mentioned, the simultaneous formation of $Mg(OH)_2$ and $MgCO_3$ occurs in the early stage of immersion (Equation (10)) in which the adsorbed Mg^+ react with OH^- and HCO_3^- ions to precipitate $Mg(OH)_2$ and $MgCO_3$ at the cathodic sites (Figure 9b). As the immersion time is prolonged, the Mg_2Ca phase at the surface was completely corroded, leaving $Mg_{17}Sr_2$ at the GBs. The dissolution of Mg_2Ca spontaneously caused the accumulation of OH^- at the $Mg_{17}Sr_2$ site readily from $Mg(OH)_2$ precipitation, in which the corrosion propagation was pinned along the GBs. Meanwhile, the $Mg(OH)_2$ precipitation continuously grows and thickens due to the continuous dissolution of Mg, which eventually covers the underlying primary corrosion precipitates and forms a dome-like structure (Figure 9c). This dome, however, can be ruptured by two factors. (i) Cl^- ions within r-SBF can infiltrate the porous $Mg(OH)_2$ dome, promoting a crevice corrosion and thus accelerating H_2 evolution at the cathodic site (HA). The rapid release of H_2 from this dome structure has ruptures the upper 'roof', leaving a volcano-like geometry, with an exposed HA structure underneath. (ii) The Cl^-

ions from the outside attack the $Mg(OH)_2$ dome, converting this structure into a highly soluble $MgCl_2$, resulting in the washed-off dome structure.

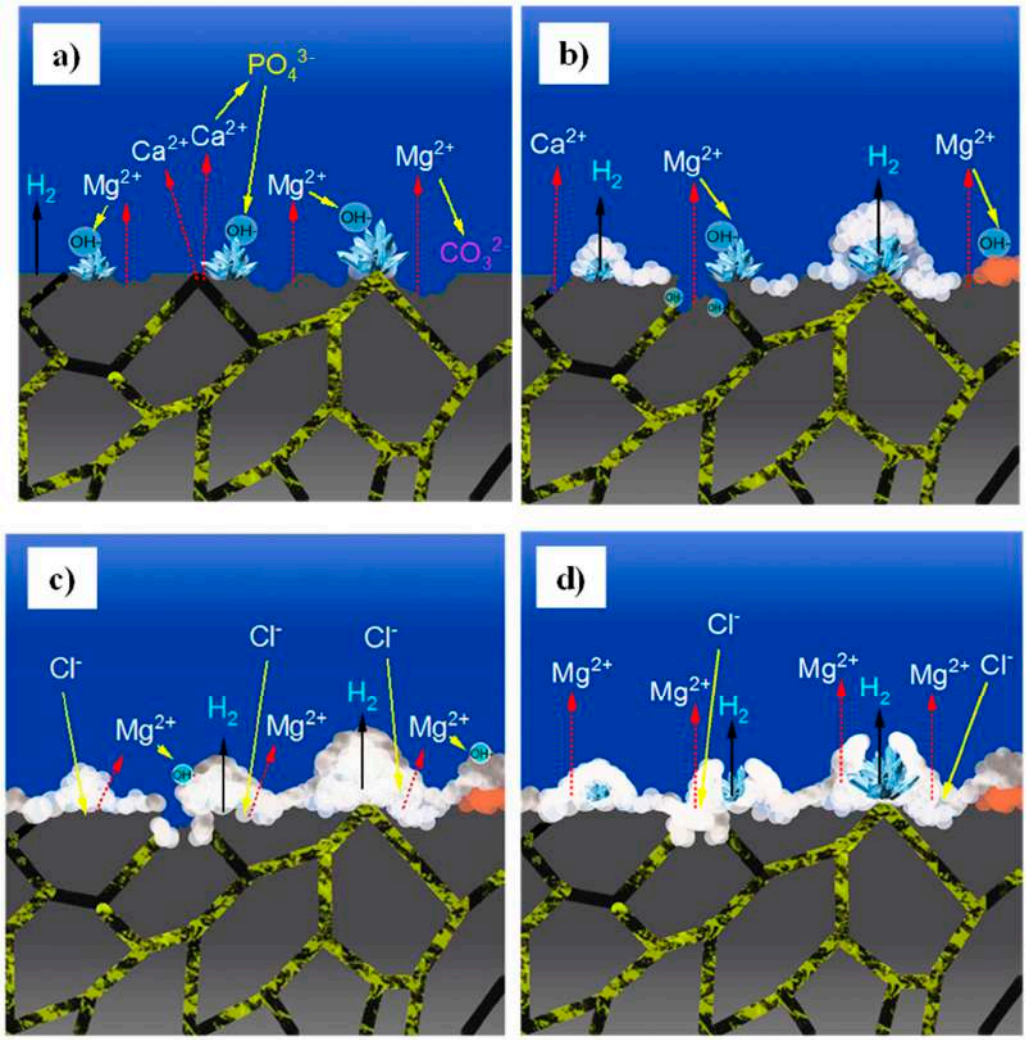

Figure 9. The schematic diagram of the Mg-1.0Ca-0.5Sr alloy corrosion mechanism in r-SBF solution; (**a**) the formation of HA structure at the cathodic site while the anodic α-Mg degrades; (**b**) the formation of whitish $Mg(OH)_2$ and orange $MgCO_3$, and the dissolution of the anodic Mg_2Ca; (**c**) the overlapping of $Mg(OH)_2$ over other precipitation due to the abundant Mg^{2+} and OH^- ions in the r-SBF and the corrosion barrier formed by $Mg_{17}Sr_2$ network, suppressing further corrosion attack within the alloy; and (**d**) the Cl^- attack and crevice corrosion exposing the underneath HA structure. The blue crystal-like structures were denoted as the HA precipitation.

4. Conclusions

The effects of corrosion media and pH-regulating techniques on CP Mg and Mg-1.0Ca-0.5Sr alloy were investigated, and the following results were concluded:

- The incorporation of Sr and Ca into the Mg-1.0Ca-0.5Sr alloy has shown an evident grain-refining effect in which its synergistic effect with the formation of secondary phases results in the enhancement in the corrosion resistance of the alloy.
- Mg_2Ca acts as a sacrificial anode, protecting or retarding the dissolution of the α-Mg; whereas the $Mg_{17}Sr_2$ cathode accelerates α-Mg dissolution in the early immersion stage but inhibits intergranular corrosion propagation by forming a continuous barrier network in the GBs.

- The dissolution of Mg_2Ca into Ca^{2+} ions near the surface facilitates the formation of a nobler HA precipitate despite the chelating reaction given by the Tris-HCL buffer reagent.
- The higher HCO_3^- content in the r-SBF (27 mM) aids in regulating the local pH value, which is confirmed by the lower pH variation in Tris-HCL buffered r-SBF, and the matched content of HCO_3^- as in the human physiological body was seen to promote the formation of stoichiometric HA deposits.
- The utilization of Tris-HCl should be avoided due to its incapability to regulate the pH near the surface of the materials, which reflects a contradicting finding across the test results. For instance, the lower pH variation in r-SBF should indicate an enhanced corrosion resistance, but it is due to the consumption of OH^- ions, which has accelerated the corrosion rate due to its precipitation-inhibiting properties. Its binding to Mg^{2+} and Ca^{2+} away from the surface of the materials has also affected the expected precipitations.
- Future work should consider chromic-cleaned surface morphology analysis because it offers conclusive evidence regarding the influence of each secondary phase on the corrosion performance of alloys based on magnesium.

Author Contributions: Conceptualization, S.S.; methodology, S.S.; software, S.S.; validation, S.S.; formal analysis, S.S.; investigation, S.S.; resources, N.H.A.N. and E.M.N.; data curation, S.S.; writing—original draft preparation, S.S.; writing—review and editing, N.H.A.N., E.M.N. and I.S.; visualization, S.S.; supervision, N.H.A.N., E.M.N. and I.S.; project administration, N.H.A.N., E.M.N., and I.S.; funding acquisition, N.H.A.N. and E.M.N. All authors have read and agreed to the published version of the manuscript.

Funding: The authors would like to acknowledge the financial support from Universiti Teknologi Malaysia for the funding under UTMShine (Q.J130000.2451.09G94), UTM R&D (R.J130000.7751.4J506), and UTM Encouragement Research Grant (Q.J130000.2651.17J44).

Data Availability Statement: Not applicable.

Acknowledgments: The authors thank Wan Mohd Mazian in the Metal Casting Laboratory for assisting with the synthesis and casting process, as well as Nurul Husna Binti Jasin of the Faculty of Bioscience and Medical Engineering and the Centre for Composite (CfC) assistant engineers for making the biocorrosion facility and their expertise available to our work. The technical support of the Materials Engineering Laboratory's assistant engineers during the metallographic analysis is gratefully acknowledged.

Conflicts of Interest: The authors declare no conflict of interest.

References

1. Fernández, J.; El Ouardi, Y.; Bonastre, J.; Molina, J.; Cases, F. Modification of the magnesium corrosion rate in physiological saline 0.9 wt% NaCl via chemical and electrochemical coating of reduced graphene oxide. *Corros. Sci.* **2019**, *152*, 75–81. [CrossRef]
2. Hanawa, T. Recent development of new alloys for biomedical use. *Mater. Sci. Forum* **2006**, *512*, 243–248. [CrossRef]
3. Xing, F.; Li, S.; Yin, D.; Xie, J.; Rommens, P.M.; Xiang, Z.; Liu, M.; Ritz, U. Recent progress in Mg-based alloys as a novel bioabsorbable biomaterials for orthopedic applications. *J. Magnes. Alloys* **2022**, *10*, 1428–1456. [CrossRef]
4. Godavitarne, C.; Robertson, A.; Peters, J.; Rogers, B. Biodegradable materials. *Orthop. Trauma* **2017**, *31*, 316–320. [CrossRef]
5. Tan, L.; Yu, X.; Wan, P.; Yang, K. Biodegradable materials for bone repairs: A review. *J. Mater. Sci. Technol.* **2013**, *29*, 503–513. [CrossRef]
6. Mei, D.; Lamaka, S.V.; Gonzalez, J.; Feyerabend, F.; Willumeit-Römer, R.; Zheludkevich, M.L. The role of individual components of simulated body fluid on the corrosion behavior of commercially pure Mg. *Corros. Sci.* **2019**, *147*, 81–93. [CrossRef]
7. Tsakiris, V.; Tardei, C.; Clicinschi, F.M. Biodegradable Mg alloys for orthopedic implants–A review. *J. Magnes. Alloys* **2021**, *9*, 1884–1905. [CrossRef]
8. Zhang, E. Phosphate treatment of magnesium alloy implants for biomedical applications. In *Surface Modification of Magnesium and Its Alloys for Biomedical Applications*; Elsevier: Amsterdam, The Netherlands, 2015; pp. 23–57.
9. Nasr Azadani, M.; Zahedi, A.; Bowoto, O.K.; Oladapo, B.I. A review of current challenges and prospects of magnesium and its alloy for bone implant applications. *Prog. Biomater.* **2022**, *11*, 1–26. [CrossRef]
10. Kumar, R.; Katyal, P. Effects of alloying elements on performance of biodegradable magnesium alloy. *Mater. Today Proc.* **2022**, *56*, 2443–2450. [CrossRef]

11. Li, H.; Lin, G.; Wang, P.; Huang, J.; Wen, C. Nutrient alloying elements in biodegradable metals: A review. *J. Mater. Chem. B* **2021**, *9*, 9806–9825. [CrossRef]
12. Maji, K.; Mondal, S. Calcium phosphate biomaterials for bone tissue engineering: Properties and relevance in bone repair. In *Racing for the Surface*; Springer: Berlin/Heidelberg, Germany, 2020; pp. 535–555.
13. Hebert, S.C. Extracellular calcium-sensing receptor: Implications for calcium and magnesium handling in the kidney. *Kidney Int.* **1996**, *50*, 2129–2139. [CrossRef] [PubMed]
14. Peacock, M. Calcium metabolism in health and disease. *Clin. J. Am. Soc. Nephrol.* **2010**, *5*, S23–S30. [CrossRef] [PubMed]
15. Mushahary, D.; Sravanthi, R.; Li, Y.; Kumar, M.J.; Harishankar, N.; Hodgson, P.D.; Wen, C.; Pande, G. Zirconium, calcium, and strontium contents in magnesium based biodegradable alloys modulate the efficiency of implant-induced osseointegration. *Int. J. Nanomed.* **2013**, *8*, 2887–2902. [CrossRef]
16. Lu, W.; Zhou, C.; Ma, Y.; Li, J.; Jiang, J.; Chen, Y.; Dong, L.; He, F. Improved osseointegration of strontium-modified titanium implants by regulating angiogenesis and macrophage polarization. *Biomater. Sci.* **2022**, *10*, 2198–2214. [CrossRef]
17. Liu, X.; Yang, H.; Xiong, P.; Li, W.; Huang, H.-H.; Zheng, Y. Comparative studies of Tris-HCl, HEPES and $NaHCO_3/CO_2$ buffer systems on the biodegradation behaviour of pure Zn in NaCl and SBF solutions. *Corros. Sci.* **2019**, *157*, 205–219. [CrossRef]
18. Oyane, A.; Kim, H.M.; Furuya, T.; Kokubo, T.; Miyazaki, T.; Nakamura, T. Preparation and assessment of revised simulated body fluids. *J. Biomed. Mater. Res. Part A* **2003**, *65*, 188–195. [CrossRef]
19. Gamble, J.L. *Chemical Anatomy, Physiology and Pathology of Extracellular Fluid: A Lecture Syllabus*; Harvard University Press: Cambridge, MA, USA, 1954.
20. Kim, H.-M.; Kishimoto, K.; Miyaji, F.; Kokubo, T.; Yao, T.; Suetsugu, Y.; Tanaka, J.; Nakamura, T. Composition and structure of apatite formed on organic polymer in simulated body fluid with a high content of carbonate ion. *J. Mater. Sci. Mater. Med.* **2000**, *11*, 421–426. [CrossRef] [PubMed]
21. Kim, H.M.; Kishimoto, K.; Miyaji, F.; Kokubo, T.; Yao, T.; Suetsugu, Y.; Tanaka, J.; Nakamura, T. Composition and structure of the apatite formed on PET substrates in SBF modified with various ionic activity products. *J. Biomed. Mater. Res.* **1999**, *46*, 228–235. [CrossRef]
22. Marco, I.; Feyerabend, F.; Willumeit-Römer, R.; Van der Biest, O. Degradation testing of Mg alloys in Dulbecco's modified eagle medium: Influence of medium sterilization. *Mater. Sci. Eng. C* **2016**, *62*, 68–78. [CrossRef]
23. Kirkland, N.; Birbilis, N.; Staiger, M. Assessing the corrosion of biodegradable magnesium implants: A critical review of current methodologies and their limitations. *Acta Biomater.* **2012**, *8*, 925–936. [CrossRef]
24. Shi, Z.; Atrens, A. An innovative specimen configuration for the study of Mg corrosion. *Corros. Sci.* **2011**, *53*, 226–246. [CrossRef]
25. Aljarrah, M.; Medraj, M. Thermodynamic modelling of the Mg–Ca, Mg–Sr, Ca–Sr and Mg–Ca–Sr systems using the modified quasichemical model. *Calphad* **2008**, *32*, 240–251. [CrossRef]
26. Bornapour, M.; Celikin, M.; Pekguleryuz, M. Thermal exposure effects on the in vitro degradation and mechanical properties of Mg–Sr and Mg–Ca–Sr biodegradable implant alloys and the role of the microstructure. *Mater. Sci. Eng. C* **2015**, *46*, 16–24. [CrossRef] [PubMed]
27. Berglund, I.S.; Brar, H.S.; Dolgova, N.; Acharya, A.P.; Keselowsky, B.G.; Sarntinoranont, M.; Manuel, M.V. Synthesis and characterization of Mg–Ca–Sr alloys for biodegradable orthopedic implant applications. *J. Biomed. Mater. Res. Part B Appl. Biomater.* **2012**, *100*, 1524–1534. [CrossRef] [PubMed]
28. Yu, H.-S.; Guo, X.-F.; Cui, H.-B. Microstructures and tensile properties of as-cast Mg-5Sn-1Si magnesium alloy modified with trace elements of Y, Bi, Sb and Sr. *China Foundry* **2021**, *18*, 9–17. [CrossRef]
29. Malekan, M.; Bahmani, A. Determination of dendrite coherency point characteristics in Al-Si-Mg alloy. *Int. J. Cast Met. Res.* **2021**, *34*, 14–20. [CrossRef]
30. Sahu, M.R.; Kumar, T.S.; Chakkingal, U. A review on recent advancements in biodegradable Mg-Ca alloys. *J. Magnes. Alloys* **2022**, *10*, 2094–2117. [CrossRef]
31. Wen, Y.; Liu, Q.; Wang, J.; Yang, Q.; Zhao, W.; Qiao, B.; Li, Y.; Jiang, D. Improving in vitro and in vivo corrosion resistance and biocompatibility of Mg–1Zn–1Sn alloys by microalloying with Sr. *Bioact. Mater.* **2021**, *6*, 4654–4669. [CrossRef]
32. Zeng, R.-C.; Qi, W.-C.; Cui, H.-Z.; Zhang, F.; Li, S.-Q.; Han, E.-H. In vitro corrosion of as-extruded Mg–Ca alloys—The influence of Ca concentration. *Corros. Sci.* **2015**, *96*, 23–31. [CrossRef]
33. Seong, J.; Kim, W. Mg–Ca binary alloy sheets with Ca contents of $\leq$ 1 wt.% with high corrosion resistance and high toughness. *Corros. Sci.* **2015**, *98*, 372–381. [CrossRef]
34. Harandi, S.E.; Mirshahi, M.; Koleini, S.; Idris, M.H.; Jafari, H.; Kadir, M.R.A. Effect of calcium content on the microstructure, hardness and in-vitro corrosion behavior of biodegradable Mg–Ca binary alloy. *Mater. Res.* **2013**, *16*, 11–18. [CrossRef]
35. Jeong, Y.; Kim, W. Enhancement of mechanical properties and corrosion resistance of Mg–Ca alloys through microstructural refinement by indirect extrusion. *Corros. Sci.* **2014**, *82*, 392–403. [CrossRef]
36. Tan, C.Y.; Singh, R.; Teh, Y.C.; Tan, Y.M.; Yap, B.K. The effects of calcium-to-phosphorus ratio on the densification and mechanical properties of hydroxyapatite ceramic. *Int. J. Appl. Ceram. Technol.* **2015**, *12*, 223–227. [CrossRef]
37. Gómez-Morales, J.; Torrent-Burgues, J.; Boix, T.; Fraile, J.; Rodríguez-Clemente, R. Precipitation of stoichiometric hydroxyapatite by a continuous method. *Cryst. Res. Technol. J. Exp. Ind. Crystallogr.* **2001**, *36*, 15–26. [CrossRef]
38. Zhou, P.; Yu, B.; Hou, Y.; Duan, G.; Yang, L.; Zhang, B.; Zhang, T.; Wang, F. Revisiting the cracking of chemical conversion coating on magnesium alloys. *Corros. Sci.* **2021**, *178*, 109069. [CrossRef]

39. Xin, Y.; Hu, T.; Chu, P.K. Degradation behaviour of pure magnesium in simulated body fluids with different concentrations of HCO_3^-. *Corros. Sci.* **2011**, *53*, 1522–1528. [CrossRef]
40. Atrens, A.; Shi, Z.; Mehreen, S.U.; Johnston, S.; Song, G.-L.; Chen, X.; Pan, F. Review of Mg alloy corrosion rates. *J. Magnes. Alloys* **2020**, *8*, 989–998. [CrossRef]
41. Atrens, A.; Johnston, S.; Shi, Z.; Dargusch, M.S. Understanding Mg corrosion in the body for biodegradable medical implants. *Scr. Mater.* **2018**, *154*, 92–100. [CrossRef]
42. Gong, C.; He, X.; Fang, D.; Liu, B.; Yan, X. Effect of second phases on discharge properties and corrosion behaviors of the Mg-Ca-Zn anodes for primary Mg-air batteries. *J. Alloys Compd.* **2021**, *861*, 158493. [CrossRef]
43. Liu, Y.; Liu, X.; Zhang, Z.; Farrell, N.; Chen, D.; Zheng, Y. Comparative, real-time in situ monitoring of galvanic corrosion in Mg-Mg_2Ca and Mg-$MgZn_2$ couples in Hank's solution. *Corros. Sci.* **2019**, *161*, 108185. [CrossRef]
44. Kondoh, K.; Takei, R.; Kariya, S.; Li, S.; Umeda, J. Local galvanic corrosion analysis on cast Mg-Ca binary alloy using scanning Kelvin probe force microscopy. *Mater. Lett.* **2022**, *319*, 132266. [CrossRef]
45. Jin, Y.; Blawert, C.; Feyerabend, F.; Bohlen, J.; Campos, M.S.; Gavras, S.; Wiese, B.; Mei, D.; Deng, M.; Yang, H. Time-sequential corrosion behaviour observation of micro-alloyed Mg-0.5 Zn-0.2 Ca alloy via a quasi-in situ approach. *Corros. Sci.* **2019**, *158*, 108096. [CrossRef]
46. Kim, J.-G.; Joo, J.-H.; Koo, S.-J. Development of high-driving potential and high-efficiency Mg-based sacrificial anodes for cathodic protection. *J. Mater. Sci. Lett.* **2000**, *19*, 477–479. [CrossRef]
47. Kim, W.-C.; Kim, J.-G.; Lee, J.-Y.; Seok, H.-K. Influence of Ca on the corrosion properties of magnesium for biomaterials. *Mater. Lett.* **2008**, *62*, 4146–4148. [CrossRef]
48. Xu, C.; Wang, J.; Chen, C.; Wang, C.; Sun, Y.; Zhu, S.; Guan, S. Initial micro-galvanic corrosion behavior between Mg_2Ca and α-Mg via quasi-in situ SEM approach and first-principles calculation. *J. Magnes. Alloys*, 2021; *in press*. [CrossRef]
49. Thekkepat, K.; Han, H.-S.; Choi, J.-W.; Lee, S.-C.; Yoon, E.S.; Li, G.; Seok, H.-K.; Kim, Y.-C.; Kim, J.-H.; Cha, P.-R. Computational design of Mg alloys with minimal galvanic corrosion. *J. Magnes. Alloys* **2022**, *10*, 1972–1980. [CrossRef]
50. Liu, H.; Zhang, K.; Yuan, J.; Li, Y.; Li, X.; Ma, M.; Shi, G.; Wang, K. In vitro degradation behavior of as-cast Mg-3Zn-1Ca-0.5 Sr alloy. *Mater. Res. Express* **2020**, *7*, 025404. [CrossRef]
51. Ding, Y.; Li, Y.; Wen, C. Effects of $Mg_{17}Sr_2$ phase on the bio-corrosion behavior of Mg–Zr–Sr alloys. *Adv. Eng. Mater.* **2016**, *18*, 259–268. [CrossRef]
52. Ascencio, M.; Pekguleryuz, M.; Omanovic, S. An investigation of the corrosion mechanisms of WE43 Mg alloy in a modified simulated body fluid solution: The effect of electrolyte renewal. *Corros. Sci.* **2015**, *91*, 297–310. [CrossRef]
53. Chelliah, N.M.; Padaikathan, P.; Kumar, R. Evaluation of electrochemical impedance and biocorrosion characteristics of as-cast and T4 heat treated AZ91 Mg-alloys in Ringer's solution. *J. Magnes. Alloys* **2019**, *7*, 134–143. [CrossRef]
54. Liang, M.-j.; Wu, C.; Ma, Y.; Wang, J.; Dong, M.; Dong, B.; Liao, H.-h.; Fan, J.; Guo, Z. Influences of aggressive ions in human plasma on the corrosion behavior of AZ80 magnesium alloy. *Mater. Sci. Eng. C* **2021**, *119*, 111521. [CrossRef] [PubMed]
55. Zhu, T.; Yu, Y.; Shen, Y.; Xiong, Y. Wear behavior of extruded ZK60 magnesium alloy in simulated body fluid with different pH values. *Mater. Chem. Phys.* **2021**, *262*, 124292. [CrossRef]
56. Bornapour, M.; Mahjoubi, H.; Vali, H.; Shum-Tim, D.; Cerruti, M.; Pekguleryuz, M. Surface characterization, in vitro and in vivo biocompatibility of Mg-0.3 Sr-0.3 Ca for temporary cardiovascular implant. *Mater. Sci. Eng. C* **2016**, *67*, 72–84. [CrossRef] [PubMed]
57. Wang, C.; Liu, X.; Mei, D.; Deng, M.; Zheng, Y.; Zheludkevich, M.L.; Lamaka, S.V. Local pH and oxygen concentration at the interface of Zn alloys in Tris-HCl or HEPES buffered Hanks' balanced salt solution. *Corros. Sci.* **2022**, *197*, 110061. [CrossRef]
58. Xin, Y.; Chu, P.K. Influence of Tris in simulated body fluid on degradation behavior of pure magnesium. *Mater. Chem. Phys.* **2010**, *124*, 33–35. [CrossRef]
59. Rad, H.R.B.; Idris, M.H.; Kadir, M.R.A.; Farahany, S. Microstructure analysis and corrosion behavior of biodegradable Mg–Ca implant alloys. *Mater. Des.* **2012**, *33*, 88–97. [CrossRef]
60. Amukarimi, S.; Mozafari, M. Biodegradable magnesium-based biomaterials: An overview of challenges and opportunities. *MedComm* **2021**, *2*, 123–144. [CrossRef]
61. Zeng, R.-C.; Hu, Y.; Guan, S.-K.; Cui, H.-Z.; Han, E.-H. Corrosion of magnesium alloy AZ31: The influence of bicarbonate, sulphate, hydrogen phosphate and dihydrogen phosphate ions in saline solution. *Corros. Sci.* **2014**, *86*, 171–182. [CrossRef]
62. Johnston, S.; Dargusch, M.; Atrens, A. Building towards a standardised approach to biocorrosion studies: A review of factors influencing Mg corrosion in vitro pertinent to in vivo corrosion. *Sci. China Mater.* **2018**, *61*, 475–500. [CrossRef]
63. Mei, D.; Lamaka, S.V.; Lu, X.; Zheludkevich, M.L. Selecting medium for corrosion testing of bioabsorbable magnesium and other metals–a critical review. *Corros. Sci.* **2020**, *171*, 108722. [CrossRef]
64. Lamaka, S.V.; Gonzalez, J.; Mei, D.; Feyerabend, F.; Willumeit-Römer, R.; Zheludkevich, M.L. Local pH and its evolution near Mg alloy surfaces exposed to simulated body fluids. *Adv. Mater. Interfaces* **2018**, *5*, 1800169. [CrossRef]
65. Mei, D.; Lamaka, S.V.; Feiler, C.; Zheludkevich, M.L. The effect of small-molecule bio-relevant organic components at low concentration on the corrosion of commercially pure Mg and Mg-0.8 Ca alloy: An overall perspective. *Corros. Sci.* **2019**, *153*, 258–271. [CrossRef]
66. McDowell, H.; Gregory, T.; Brown, W. Solubility of $Ca_5(PO_4)_3OH$ in the system $Ca(OH)_2$-H_3PO_4-H_2O at 5, 15, 25, and 37 °C. *J. Res. Natl. Bur. Standards. Sect. A Phys. Chem.* **1977**, *81*, 273. [CrossRef]
67. Xin, Y.; Huo, K.; Tao, H.; Tang, G.; Chu, P.K. Influence of aggressive ions on the degradation behavior of biomedical magnesium alloy in physiological environment. *Acta Biomater.* **2008**, *4*, 2008–2015. [CrossRef]

68. Brady, M.; Rother, G.; Anovitz, L.; Littrell, K.; Unocic, K.; Elsentriecy, H.; Song, G.-L.; Thomson, J.; Gallego, N.; Davis, B. Film breakdown and nano-porous $Mg(OH)_2$ formation from corrosion of magnesium alloys in salt solutions. *J. Electrochem. Soc.* **2015**, *162*, C140. [CrossRef]
69. Maltseva, A.; Shkirskiy, V.; Lefèvre, G.; Volovitch, P. Effect of pH on Mg (OH) 2 film evolution on corroding Mg by in situ kinetic Raman mapping (KRM). *Corros. Sci.* **2019**, *153*, 272–282. [CrossRef]
70. Ott, N.; Schmutz, P.; Ludwig, C.; Ulrich, A. Local, element-specific and time-resolved dissolution processes on a Mg–Y–RE alloy–Influence of inorganic species and buffering systems. *Corros. Sci.* **2013**, *75*, 201–211. [CrossRef]
71. Ferreira, C.M.; Pinto, I.S.; Soares, E.V.; Soares, H.M. (Un) suitability of the use of pH buffers in biological, biochemical and environmental studies and their interaction with metal ions—A review. *Rsc Adv.* **2015**, *5*, 30989–31003. [CrossRef]